

Programming Nonlinear Interfacial Mechanics of Synthetic Cells: Lipid Geometry and DNA Nanostructures

Kazutoshi Masuda¹ | Miho Yanagisawa^{1,2,3}

¹Komaba Institute for Science, Graduate School of Arts and Sciences, The University of Tokyo, Komaba 3-8-1, Meguro, Tokyo 153-8902, Japan

²Department of Physics, Graduate School of Science, The University of Tokyo, Hongo 7-3-1, Bunkyo, Tokyo 113-0033, Japan

³Center for Complex Systems Biology, Universal Biology Institute, The University of Tokyo, Komaba 3-8-1, Meguro, Tokyo 153-8902, Japan

Correspondence

Miho Yanagisawa, Kazutoshi Masuda
Email:
(M. Y.) myanagisawa@g.ecc.u-tokyo.ac.jp
(K. M.) kazumassuu@g.ecc.u-tokyo.ac.jp

Funding information

Soft interfaces formed by lipid membranes are fundamental to living cells, synthetic cells, and membrane-based soft materials. However, a quantitative framework linking molecular organization with nonlinear interfacial mechanics remains elusive. Here, we establish an analytical framework that captures the nonlinear elastic response of lipid-membrane-coated synthetic cells under micropipette aspiration. Incorporating both area stretching and curvature bending enables the model to quantitatively reproduce the complete pressure–displacement response within the small-deformation regime. This approach reduces interfacial mechanics to two parameters: the in-plane area-stretching modulus and an out-of-plane bending-related term. Using this unified framework, we experimentally demonstrate that nonlinear interfacial mechanics can be programmed by altering the molecular geometry and effective dimensionality of adsorbed elements. The lipid molecular shape and curvature-dependent packing regulate in-plane stiffness, while DNA nanostructures, the other adsorbed element, introduce an orthogonal control axis via dimensionality: isolated motifs primarily enhance area stretching, whereas three-dimensional network architectures markedly reinforce bending resistance. Together, these results establish a general molecular design principle for programming interfacial mechanics and pro-

vide a quantitative foundation for engineering mechanically tunable synthetic cells and soft interfaces.

1 | INTRODUCTION

Soft interfaces formed by lipid membranes are fundamental building blocks of living cells, synthetic cells, and membrane-based soft materials [1, 2, 3]. In biological systems, lipid membranes provide structural integrity while enabling dynamic mechanical regulation and biochemical activity within cells [4]. Beyond biology, lipid-coated droplets and liposomes have emerged as versatile platforms for synthetic cells, soft microcapsules, and biomedical applications, including drug delivery capsules [5]. Across these systems, functionality is closely tied to mechanical response, positioning lipid-based interfaces as a prototypical class of soft matter characterized by nonlinear interfacial mechanics.

Despite their broad relevance, a quantitative understanding of how molecular organization controls nonlinear interfacial mechanics remains limited. Interfacial mechanical properties do not arise solely from the chemical identity of lipids, but instead emerge from collective molecular features such as geometry [6, 7], packing density [8, 9, 10], and the presence of additional components localized at or beneath the interface [11, 12]. DNA nanostructures are particularly attractive in this context, as their geometry and connectivity can be programmed with molecular precision [13, 14]. This capability opens new opportunities for material design [15], while simultaneously raising a fundamental question that spans soft-matter physics, biophysics, and materials science: how do the geometry and effective dimensionality of adsorbed molecular elements determine the emergent mechanics of soft interfaces?

Addressing this question requires both reliable experimental access and a physically based framework of interpreting deformation. Micropipette aspiration is a powerful method for probing the mechanics of soft, cell-like systems by directly relating applied pressure to interfacial deformation [16, 17, 18]. Although theoretical descriptions exist for large deformations, whether static or time-dependent [19, 20], analytical models that capture small yet nonlinear deformations remain limited. In practice, experimental aspiration data are often analyzed using conventional models, such as the half-space model [21] or the classic Young–Laplace law [22], which estimate elastic moduli or interfacial tension by fitting only the linear regime of the deformation process. Therefore, the pronounced nonlinear response observed at minimal deformations is typically neglected. A key limitation of these conventional models is that they do not explicitly incorporate not thermal but curvature-induced bending elasticity, despite its central role in theoretical and computational descriptions of soft interfaces, including lipid membranes [23, 24]. Such approaches fail to capture the interfacial mechanics of lipid membranes with intrinsic molecular curvature or those of membranes functionalized with nanostructures possessing finite rigidity. Consequently, existing analytical frameworks remain insufficient for quantitatively describing the early nonlinear mechanical response of lipid-based soft interfaces.

Here, we introduce a physics-based analytical framework that quantitatively captures the nonlinear deformation of lipid-membrane-coated synthetic cells under aspiration. By integrating area stretching and curvature elasticity, the model reproduces the full pressure–displacement response before large deformation with viscous flow. It reduces interfacial mechanics to two physically meaningful parameters: an in-plane area-stretching modulus and an out-of-plane bending-related term. Using this unified framework, we demonstrate that nonlinear interfacial mechanics can be rationally programmed through a common physical principle: the molecular geometry, effective packing density, and dimensionality of adsorbed elements. Lipid geometry and packing density selectively regulate in-plane stiffness. In contrast, DNA nanostructures introduce an orthogonal control axis via their dimensionality, with isolated motifs enhancing area stretching and three-dimensional networks reinforcing bending resistance. Together, these results establish a general strategy for engineering mechanically programmable soft interfaces and synthetic cells.

2 | ANALYTICAL MODEL FOR NONLINEAR ELASTIC RESPONSE

2.1 | Energy change of elastic shells due to pipette aspiration deformation

To analyze the interfacial mechanical properties of spherical droplets coated with a lipid monolayer, which serve as simple synthetic cells, we employed a classical pipette aspiration setup, as illustrated in Figure 1a. In this configuration, a pressure difference P between the interior and exterior of the pipette with an inner radius R_p , deforms the membrane, pulling it into the pipette by a length L . We focus on the regime of small deformations, where the aspiration length is normalized by the pipette radius,

$$x \equiv \frac{L}{R_p}, \quad (1)$$

remains below unity. In this regime ($x < 1$), deformations outside the pipette can be neglected (see Figure S1 in the Supporting Information), and the mechanical response is governed primarily by the energies of the aspirated region.

To analyze the experimentally obtained nonlinear P - x curves, we consider the change in elastic energy associated with aspiration, which consists of the area-stretching energy due to changes in the membrane surface area, $\Delta E_{\text{stretch}}$, and the bending energy arising from curvature variations, ΔE_{bend} :

$$\Delta E_{\text{stretch}} + \Delta E_{\text{bend}} = \int_{x_0}^x P_{\text{diff}}(x) \frac{dV}{dx} dx. \quad (2)$$

Here, $P_{\text{diff}}(x)$ denotes the effective pressure difference, which will be described in detail below. The parameter x_0 is the initial normalized aspiration length originating from the intrinsic curvature of the droplet.

The volume V and surface area A of the aspirated region are given geometrically as (see Section S1 for details):

$$V = \frac{\pi R_p^3}{6} (3x + x^3), \quad (3)$$

$$A = \pi R_p^2 (1 + x^2). \quad (4)$$

2.2 | Area-stretching energy

When considering area stretching of a lipid monolayer membrane, two distinct molecular-level scenarios arise depending on the rate at which lipids are supplied from the reservoir, as illustrated in Figure 1b. If the characteristic timescale of aspiration-induced deformation is sufficiently long compared to the lipid supply timescale, the newly created interface is rapidly populated by lipid molecules and reaches a quasi-equilibrium state. Under this condition, the interfacial tension remains constant at its equilibrium value, $\gamma = \gamma_0$ (Figure 1b, upper). In contrast, when the deformation occurs on a shorter timescale, the number of lipid molecules that can adsorb to the expanding interface during deformation is limited. As a result, γ cannot equilibrate instantaneously and instead evolves dynamically with time (Figure 1b, lower).

For synthetic cells such as droplets and liposomes, the supply of lipids typically occurs on timescales longer than ~ 1 s [25], which is comparable to the aspiration timescale used in this study. We therefore adopt the latter scenario with a time-varying interfacial tension.

Assuming uniform strain in the aspirated region, the area-stretching modulus K is treated as constant, and the

interfacial tension γ is expressed as a function of the areal strain

$$\varepsilon_A \equiv \frac{A - A_0}{A_0}, \quad (5)$$

as

$$\gamma(x) = \gamma_0 + K\varepsilon_A = (\gamma_0 - K) + K \frac{A}{A_0}, \quad (6)$$

where γ_0 and A_0 denote the interfacial tension and area prior to aspiration, respectively.

The area-stretching energy is then calculated by integrating γ over the aspirated surface area:

$$E_{\text{stretch}} = \int \gamma \, dA = (\gamma_0 - K)A + \frac{K}{2} \frac{A^2}{A_0}. \quad (7)$$

2.3 | Bending energy

According to the classical description of membrane bending rigidity [26], the bending energy associated with curvature deformations is given by

$$E_{\text{bend}} = \int 2k (H - c_0)^2 \, dA, \quad (8)$$

where k is the bending modulus, H is the mean curvature, and c_0 is the spontaneous curvature of the membrane.

In our lipid monolayer system, c_0 is primarily determined by the molecular geometry of the lipids coating the droplet. During pipette aspiration, curvature variations mainly arise in two regions: the aspirated spherical segment inside the pipette and the pipette edge (Figure 1c).

For the aspirated spherical region, the radius of curvature is

$$R' = R_p \frac{1 + x^2}{2x}. \quad (9)$$

The corresponding bending energy is

$$\begin{aligned} E_{\text{sphere}} &= 2k A \left(\frac{1}{R'} - \frac{1}{R_0} \right)^2 \\ &\approx \frac{\pi k}{2} \left(\frac{R_p}{R_0} \right)^2 (1 + x^2) = O\left(\frac{R_p^2}{R_0^2} \right), \end{aligned} \quad (10)$$

where R_0 is the intrinsic curvature radius defined by $c_0 = 1/R_0$.

At the pipette edge, the membrane curvature is much larger than that of the spherical regions and is governed by the monolayer thickness $h \ll R_p$. Approximating this junction as an axisymmetric surface of revolution with a characteristic curvature of order $(h/2)^{-1}$ (Figure 1c), and using the geometric condition $h, R_0 \ll R'$, the bending

energy at the edge is estimated as (see Section S2)

$$\begin{aligned} E_{\text{edge}} &\approx 2kA_{\text{edge}} \left[\frac{1}{2} \left(\frac{1}{h/2} - \frac{1}{R_p} \right) - \frac{1}{R_0} \right]^2 \\ &\approx \frac{k}{2} A_{\text{edge}} \left(\frac{1}{h/2} - \frac{2}{R_0} \right)^2 = O\left(\frac{R_p}{h}\right). \end{aligned} \quad (11)$$

Because h and R_0 are on the nanometer scale, whereas R_p is on the micrometer scale, we obtain $E_{\text{edge}} \ll E_{\text{sphere}}$. The contribution from the pipette edge can therefore be neglected.

2.4 | Expression of experimentally obtained force curve

From Equations 2, 7, and 10, the effective pressure difference between the interior of the pipette and that of the droplet is given by

$$P_{\text{diff}}(x) = \frac{4}{R_p} \left[\frac{K}{1+x_0^2} x + (\gamma_0 - K) \frac{x}{1+x^2} \right] + \frac{2k}{R_p R_0^2} \frac{x}{1+x^2}. \quad (12)$$

To compare with the experimentally obtained P - x curve, the effective pressure difference $P_{\text{diff}}(x)$ was adjusted by subtracting the contributions from interfacial tension, referred to as Young–Laplace pressure, and from the restoring pressure resulting from droplet bending outside the pipette [27, 28] (see Section S3):

$$P(x) = P_{\text{diff}}(x) - \left[\frac{2\gamma(x)}{R} + \frac{k}{R} \left(\frac{1}{R_0} \right)^2 \right]. \quad (13)$$

Combining Equations 12 and 13, we finally obtain

$$P(x) = \frac{4}{R_p} \left(\gamma_0 + \frac{k}{2R_0^2} + K \frac{x^2 - x_0^2}{1+x_0^2} \right) \left(\frac{x}{1+x^2} - \frac{R_p}{2R} \right), \quad (14)$$

which contains two fitting parameters, $\gamma_0 + k/(2R_0^2) \equiv \gamma_0 + \tilde{k}$ and K . Depending on these parameters, the model reproduces both convex-downward and convex-upward P - x curves (Figure 1d and Figure S2).

3 | RESULTS AND DISCUSSION

3.1 | Experimental Validation of the Analytical Model

Before investigating the effects of lipids and DNA nanostructures on the interfacial mechanics of synthetic cells, we first validated the proposed analytical model (Equation 14) using droplets coated with a lipid monolayer. These droplets provide a well-defined and controllable model system, enabling direct comparison between experimental measurements and theoretical predictions. Figure 1d displays two representative pressure–displacement (P - x) curves obtained from pipette aspiration, exhibiting either downward-convex (upper) or upward-convex (lower) behavior. The analytical model (solid lines) quantitatively reproduces the experimental data over the entire displacement range for both response types ($R^2 = 0.99 \pm 0.03$, mean \pm s.d.). Notably, the model captures both convex and concave nonlinearities within a single unified framework, a capability that conventional approaches cannot achieve. In contrast, the conven-

tional Young–Laplace fitting assumes a constant interfacial tension γ_0 (dashed lines) and shows systematic deviations. This is especially apparent for downward-convex responses and at larger displacements ($R^2 = 0.94 \pm 0.07$, mean \pm s.d.). Neglecting the elastic contribution in the modified Young–Laplace pressure (Equation 13) further worsens the fitting quality. This result underscores the necessity of incorporating elastic effects. Together, these results confirm the validity of the proposed analytical framework and establish a reliable basis for subsequent analysis of how lipid composition and DNA nanostructure modulate the mechanical properties of droplets as synthetic cell models.

3.2 | Lipid-Dependent Interfacial Mechanics of Synthetic Cell Droplets

To compare the interfacial mechanics of lipid-monolayer-coated droplets, we examined four lipids with distinct headgroup charges: PG (negatively charged), PC and PE (electrically neutral), and TAP (positively charged) (see Experimental section for details). Aspiration of the droplets yielded the P – x curves for each lipid, as presented in Figure 2a and b. These nonlinear curves were obtained at the regime of relatively small deformation that precedes the onset of viscous flow in the large-deformation region. Regardless of headgroup charge, all lipids exhibit upward convex P – x curves that are accurately described by the model using Equation 14.

Under identical aspiration lengths x , droplets coated with PE (green) and TAP (pink) required substantially higher aspiration pressures than those coated with PC (orange) and PG (blue) (Figure 2c), revealing pronounced lipid-dependent differences in interfacial mechanical response. To quantify these differences, we fitted each P – x curve using Equation 14 and extracted the area-stretching modulus K and the bending-related term $\gamma_0 + \tilde{\kappa}$. Both parameters were largest for PE (electrically neutral), followed by TAP (positively charged), PC (electrically neutral), and PG (negatively charged) (Figure 2d). The magnitude of the extracted area-stretching modulus K is consistent with values reported for related lipid-coated interfaces. For example, oscillatory deformation measurements of oil–water interfaces stabilized by a lipid monolayer have reported K values on the order of 1 mN m^{-1} [7], comparable to those obtained here. This agreement supports the physical validity of the extracted parameters and demonstrates that the present model yields quantitatively reasonable mechanical moduli.

The systematic ordering of the two extracted mechanical parameters, with PE exhibiting markedly higher values than the other lipids, cannot be attributed to headgroup charge but instead can reflect intrinsic differences in lipid molecular geometry. Such geometry is commonly characterized by the spontaneous curvature c_0 , which arises from a mismatch between the cross-sectional areas of the lipid headgroup and hydrophobic tail. As illustrated in Figure 2e, cylindrical lipids such as PC, PG, and TAP possess near-zero spontaneous curvature and therefore favor planar monolayer configurations. In contrast, PE has an inverted-cone molecular shape with a negative spontaneous curvature ($c_0 < 0$) [29], originating from its relatively small headgroup compared to the hydrophobic tail, and thus intrinsically prefers membranes curved toward the hydrophilic side.

We first address why PE exhibits a substantially larger K than the other lipids, focusing on molecular geometry, spontaneous curvature, and the resulting in-plane packing of the lipid monolayer. The modulus K quantifies the free-energy penalty associated with lateral area expansion of the membrane, which requires separation of neighboring lipid molecules within the interfacial plane. Lipid planar membranes with stronger in-plane cohesion and higher packing density, therefore, exhibit larger values of K [30]. Such packing characteristics are intrinsically linked to lipid molecular geometry, as encoded by the spontaneous curvature c_0 . In contrast to cylindrical lipids with near-zero c_0 , inverted cone-shaped lipids with non-zero spontaneous curvature, such as PE, tend to pack more densely within the interfacial plane when constrained to form a curved monolayer (Figure 2e). This enhanced packing on the curved membrane leads to a higher energetic cost upon lateral expansion, resulting in an increased K . Consistent with this interpretation, cone-shaped lipids with non-zero spontaneous curvature, including PE, have been reported to exhibit enhanced in-plane

cohesion and ordering compared with cylindrical lipids, as evidenced by increased rigidity in Langmuir monolayer compressibility measurements and interfacial rheology studies [31, 32]. These results demonstrate that, even in three-dimensionally closed membranes such as synthetic cells, in-plane lipid packing, which depends on lipid geometry, plays a dominant role in governing resistance to lateral deformation.

We next examine why PE also exhibits a substantially larger value of $\gamma_0 + \tilde{\kappa}$ compared with the other lipids. The first contribution, the interfacial tension γ_0 , represents the free energy of the oil–water interface covered by a lipid monolayer. In general, adsorption of amphiphilic molecules reduces γ_0 as the interfacial adsorption density increases. In contrast, the bending-related contribution $\tilde{\kappa}$ has been reported to increase with increasing adsorption density, reflecting enhanced resistance to curvature deformation [33, 34]. As a result, the composite parameter $\gamma_0 + \tilde{\kappa}$ is expected to exhibit a weak or negligible dependence on the lipid adsorption density due to these opposing trends and $\tilde{\kappa}$ is maximized under lipid saturation (Figure 2f).

To test whether the markedly larger $\gamma_0 + \tilde{\kappa}$ observed for PE arises from incomplete interfacial saturation, we increased the lipid concentration in the oil phase from 1 mM (above the critical micelle concentration) to 2 mM. No statistically significant changes were detected in either fitted parameters (Figure 2g), indicating that the oil–water interface is already saturated at 1 mM under the present conditions. Independent interfacial tension measurements using the Wilhelmy plate method have reported that PE exhibits a higher equilibrium tension γ_0 than cylindrical lipids [35], consistent with a dominant contribution from its intrinsic molecular geometry.

We further analyzed the droplet-size dependence to disentangle the relative contributions of interfacial tension and bending elasticity (Figure 2h). The composite parameter $\gamma_0 + \tilde{\kappa}$ remains nearly independent of $1/R$ over the entire size range investigated. This size invariance suggests that the changes in γ_0 and $\tilde{\kappa}$ caused by the shift in effective adsorption packing compensate each other as the droplet curvature changes. In contrast, the area-stretching modulus K of PE exhibits a pronounced size dependence: while K remains constant for $1/R \geq 0.02 \mu\text{m}^{-1}$ (corresponding to $R \leq 50 \mu\text{m}$), it decreases systematically for larger droplets with lower curvature (no comparable size dependence for the other lipids; Figure S3).

This behavior can be rationalized by considering the intrinsic negative spontaneous curvature of PE. For μm -sized droplets, the membrane surface appears nearly planar on the molecular length scale. As a result, PE molecules, which favor curved configurations ($c_0 < 0$), experience packing frustration on flatter, larger droplets, leading to a reduced packing density and a smaller apparent K . Although such reduced packing would tend to increase γ_0 due to a lower effective adsorption packing density, it concurrently reduces the bending contribution $\tilde{\kappa}$, yielding an approximately constant value of $\gamma_0 + \tilde{\kappa}$. These findings indicate that the enhanced $\gamma_0 + \tilde{\kappa}$ observed for PE is primarily due to the bending contribution of PE membrane under highly packed conditions resulting from its inverted-cone shape. In addition, the inverted-cone shape of PE exhibits stable and well-defined mechanical behavior only above a threshold curvature, which under the present conditions corresponds to $1/R \geq 0.02 \mu\text{m}^{-1}$, since inefficient packing limits membrane integrity at the low-curvature interfaces of large droplets.

3.3 | DNA-Nanostructure-Induced Modulation of Interfacial Mechanics

To quantitatively assess how the adsorption of DNA nanostructures modulates the interfacial mechanics of droplets, we encapsulated self-assembled DNA motifs within droplets coated with a cationic TAP monolayer and performed micropipette aspiration experiments. Three partially complementary DNA strands were annealed to form Y-shaped motifs. By introducing terminal sticky ends, we generated cross-linked networks (Y4) and compared them with isolated motifs without the sticky ends (Y0, Figure 3a). Owing to their negative charge, the DNA motifs are electrostatically attracted to the positively charged TAP monolayer and localize beneath the droplet interface [36].

At identical aspiration lengths x , droplets containing Y4 required higher aspiration pressures than those containing Y0 (Figure 3b), indicating that DNA's network formation enhances interfacial resistance to deformation. To quantify these effects, the pressure-displacement curves were fitted using Equation 14, yielding the area-stretching modulus K and the bending-related term $\gamma_0 + \tilde{k}$. The modulus K was highest for Y0, whereas Y4 and the DNA-free control exhibited comparable values (Figure 3c, left). In contrast, $\gamma_0 + \tilde{k}$ increased monotonically from the DNA-free condition (1 mM TAP) to Y0 and was largest for Y4 (Figure 3c, right). It should be noted that the aqueous phase here contained Tris-HCl buffer rather than the NaCl solution used droplets without DNA (shown in Figure 2).

We first consider the behavior of K . Comparison between Y0-containing and DNA-free droplets shows that adsorption of DNA motifs significantly enhances the in-plane stiffness of the monolayer. This result is notable, as reinforcement of membrane mechanics in both biological and synthetic cells typically relies on polymeric or cytoskeleton networks [37, 38]. Here, isolated DNA motifs increase lateral resistance solely through interfacial adsorption, without forming an extended network. The lower K observed for Y4 compared with Y0 indicates that sticky-end-mediated crosslinking reduces the effective surface density of DNA motifs directly adsorbed at the interface. Although the Y4 motifs are electrostatically localized near the membrane, their preassembled three-dimensional network structure prevents efficient flattening into a quasi-two-dimensional layer (Figure 3d). With an interaction energy on the order of $\sim 10 k_B T$ per junction and a mesh size of ~ 20 nm, flattening the network would require substantial deformation or rupture of multiple cross-links, which is energetically unfavorable. As a result, only a fraction of motifs can directly contribute to area stretching, leading to a reduced apparent K . This mechanism parallels the lipid-dependent behavior discussed above, in which reducing the effective packing density decreases the magnitude of K .

We next consider the bending-related term $\gamma_0 + \tilde{k}$. Comparison between Y0 and DNA-free droplets shows that adsorption of DNA motifs substantially increases $\gamma_0 + \tilde{k}$, i. e., enhancing resistance to out-of-plane deformation. Because the persistence length of double-stranded DNA (~ 50 nm) exceeds the characteristic dimensions of the DNA motifs, the adsorbed DNA motifs behave as rigid inclusions that enhance the bending rigidity of the interface. Notably, $\gamma_0 + \tilde{k}$ further increased for Y4 compared with Y0, despite a reduction in the packing density inferred from the lower K of Y4 than Y0. This result highlights that $\gamma_0 + \tilde{k}$ for Y4 is predominantly governed by the bending \tilde{k} rather than the tension contribution. In other words, while K primarily reflects the two-dimensional packing density of DNA motifs directly adsorbed at the interface, \tilde{k} is governed by the mechanical rigidity and finite thickness of the three-dimensional DNA network located beneath the lipid membrane.

To derive the mechanical properties of the three-dimensional structure of the Y4 DNA on the lipid membrane in more detail, we plotted the correlation between the two extracted parameters, and compared them with those of various two-dimensional systems: lipid-only membrane (the same data shown in Figure 2d) and a lipid membrane plus Y0 DNA (Figure 3e). According to thin film theory, the bending rigidity k is proportional to the cube of the membrane thickness, while the areal stretching coefficient K is proportional to the thickness [39]. Therefore, excluding thickness, we obtain a scaling relationship of the form $k \propto K^3$. For all systems except Y4 DNA, the measured mean values align with a single scaling curve proportional to K^3 (indicated by a gray line in Figure 3e). This observation indicates that the mechanically effective membrane thickness remains approximately constant across these lipid systems, regardless of the presence of Y0 DNA. Additionally, the results indicate that the elastic contribution \tilde{k} predominates in the composite parameter $\gamma_0 + \tilde{k}$, as noted above. Thus, for droplets coated with spontaneously adsorbed elements, the interfacial mechanics are governed primarily by the packing density of elements directly adsorbed at the membrane. In contrast, Y4 forms a three-dimensional DNA network, resulting in an effective membrane thickness that is significantly greater than that of lipid-only membranes or those decorated with Y0. Consistent with this expectation, the Y4 data points deviate markedly from the common scaling curve.

These results demonstrate that even for identical DNA nanostructures, the mechanical contribution to the in-

terface depends fundamentally on whether they exist as isolated motifs (Y0) or as a crosslinked three-dimensional network (Y4). The former primarily enhances resistance to area stretching, whereas the latter, by acting as a finite-thickness structure, dominantly increases resistance to bending deformations. Moreover, our findings indicate that introducing three-dimensional network architectures into synthetic cells is an effective strategy for selectively enhancing bending resistance in the direction normal to the interface, as reflected by an increased $\tilde{\kappa}$.

Finally, we estimate the bending rigidity k of droplets bearing a three-dimensional Y4 DNA network beneath the lipid membrane. The spontaneous curvature of PE has been reported to lie in the range $c_0 \approx -0.05$ to -0.03 nm^{-1} [29]; here, we adopt a representative value of $c_0 = -0.04 \text{ nm}^{-1}$. From the experimental fitting, the bending-related term $\tilde{\kappa}$ is on the order of $\sim 1 \text{ mN m}^{-1}$. Using the relation $\tilde{\kappa} = k/(2R_0^2) = kc_0^2/2$, we estimate the bending rigidity of droplets with the Y4 DNA network to be $k \sim 10^2 k_B T$. This value is approximately five times larger than that obtained for droplets without DNA or with isolated Y0 DNA motifs (Figure 3e), indicating a substantial enhancement in bending rigidity induced by the three-dimensional DNA network. Notably, the estimated magnitude is comparable to reported bending rigidities of red blood cell membranes, which span from a few to $\sim 10^2 k_B T$ depending on measurement conditions [40]. This quantitative agreement underscores that adsorption of a finite-thickness DNA network beneath a lipid membrane can endow synthetic cells with bending mechanics approaching those of biological membranes.

4 | CONCLUSION

In this study, we established a quantitative, unified framework for describing the nonlinear interfacial mechanics of lipid-membrane-coated droplets, serving as synthetic cells, by combining systematic micropipette aspiration experiments with a physically based analytical model. By explicitly incorporating both area stretching and bending rigidity into the description of aspiration deformation, the proposed model quantitatively reproduces the full pressure–displacement (P – x) response in the small but nonlinear regime preceding viscous flow. This combined experimental-theoretical approach reduces interfacial mechanics to two physically interpretable parameters: the area-stretching modulus K , which captures in-plane resistance, and a composite interfacial-tension and bending-related term, $\gamma_0 + \tilde{\kappa}$, governing out-of-plane deformation.

Using these experimentally accessible parameters as a common mechanical metric, we demonstrate that interfacial mechanics across chemically distinct systems can be understood within a shared physical framework. For lipid monolayers, intrinsic molecular curvature and packing constraints jointly regulate mechanical response. Inverted-cone-shaped PE, characterized by a large negative spontaneous curvature, exhibits substantially enhanced values of both K and $\gamma_0 + \tilde{\kappa}$ compared with cylindrical lipids such as PC, PG, and TAP. Concentration- and size-dependent measurements, made interpretable by the analytical model, further reveal that interfacial packing selectively modulates K , whereas $\gamma_0 + \tilde{\kappa}$ remains largely insensitive to droplet size, consistent with its bending contribution.

Extending this experimentally validated framework to DNA-functionalized interfaces reveals an additional, orthogonal mechanism for mechanical control that arises from dimensionality. Isolated DNA motifs (Y0) behave as quasi-two-dimensional adsorbates that primarily enhance in-plane stiffness by increasing K through direct interfacial coupling. In contrast, cross-linked DNA nanostructures (Y4) form a finite-thickness three-dimensional network beneath the lipid monolayer, which is directly captured by the model as a pronounced increase in $\gamma_0 + \tilde{\kappa}$, reflecting enhanced resistance to bending even at reduced effective interfacial adsorption density.

Together, these results demonstrate that only by integrating quantitative experiments with an analytical description of nonlinear deformation can one directly link molecular-scale organization to emergent interfacial mechanics. This work establishes a general design principle for soft interfaces, in which in-plane and out-of-plane mechanical

properties can be independently and predictably programmed by controlling molecular geometry, effective surface density, and the dimensionality of adsorbed components. By providing a unified physical framework that connects molecular design to nonlinear mechanical function, our study lays the foundation for the rational engineering of mechanically programmable synthetic cells, membrane-based soft materials, and biomimetic systems whose functionality is encoded in interfacial mechanics.

5 | MATERIALS AND METHODS

5.1 | Materials

1,2-dioleoyl-sn-glycero-3-phosphoglycerol (PG), 1,2-dioleoyl-sn-glycero-3-phosphocholine (PC), 1,2-dioleoyl-sn-glycero-3-phosphoethanolamine (PE), and 1,2-dioleoyl-3-trimethylammonium-propane (TAP; chloride salt) were purchased from Avanti Polar Lipids. Lipids were dissolved in chloroform (Nacalai Tesque), and lipid films obtained after solvent evaporation were redissolved in hexadecane (Nacalai Tesque) as the oil phase. Sodium chloride (NaCl; FUJIFILM Wako Pure Chemical Co.) and Tris-HCl buffer (pH 8.0; Nacalai Tesque) were dissolved in ultrapure water (Invitrogen) to prepare the aqueous phase. For experiments involving DNA motifs, lyophilized DNA oligonucleotides (salt-free grade; Eurofins Genomics Japan) were dissolved in ultrapure water and added to the aqueous phase as appropriate. DNA stock solutions were prepared at 2 mM and stored at -20 °C until use. All materials were used as received without further purification.

5.2 | Droplet preparation

Water-in-oil droplets encapsulated by lipid monolayers were prepared as follows. Lipids were first dissolved in chloroform at a final concentration of 10 mM. An aliquot (50 μ L) of the lipid solution was transferred to a Durham tube, and the solvent was evaporated under a gentle stream of nitrogen gas to form a dry lipid film at the bottom of the tube. Hexadecane (500 μ L) was then added, and the mixture was sonicated at approximately 60 °C for 90 min to obtain a lipid-in-oil solution with a final lipid concentration of 1 mM. The solution was subsequently cooled slowly from 60 °C to room temperature (approximately 25 °C) with intermittent vortex mixing to ensure homogeneous lipid dissolution.

The aqueous phase consisted of a 370 mM NaCl solution, unless otherwise noted. For experiments involving DNA nanostructures, the composition of the aqueous phase was modified as described in the following section. To generate droplets, 2 μ L of the aqueous phase was added to 40 μ L of the lipid-in-hexadecane solution after sonication, and the mixture was gently tapped to induce droplet formation without bulk emulsification. The resulting droplets were transferred onto a silicone-coated glass-bottom dish (Matsunami) to prevent adhesion to the glass surface and were used for subsequent observations and measurements.

5.3 | DNA nanostructure preparation

DNA oligomers were designed based on a previously reported architecture to assemble into Y-shaped DNA nanostructures [36]. At high temperatures, the DNA oligomers remain dissociated due to entropic stabilization, whereas upon cooling they hybridize via Watson-Crick base pairing to form Y-shaped motifs. Two types of DNA nanostructures were prepared: motifs bearing sticky ends at the three termini (G1-G3) and motifs without sticky ends (S1-S3) (Figure S4). Upon further cooling, the sticky-end-bearing nanostructures undergo additional hybridization between complementary sticky ends, resulting in the formation of extended network structures, whereas nanostructures with-

out sticky ends do not form networks.

DNA nanostructures with sticky ends (G1–G3) exhibit two characteristic melting transitions. Specifically, Y-shaped motifs are formed below the first melting temperature, T_{m1} , followed by inter-motif hybridization via sticky ends at the second melting temperature, T_{m2} . In contrast, nanostructures without sticky ends (S1–S3) display a single melting transition at T_{m1} and remain as isolated motifs. The melting temperatures were $T_{m1} = 69\text{ }^{\circ}\text{C}$ and $T_{m2} = 49\text{ }^{\circ}\text{C}$.

For self-assembly, the constituent DNA oligomers were mixed at equimolar ratios and diluted in buffer (20 mM Tris–HCl, pH 8.0, 350 mM NaCl) to a final DNA concentration of approximately 5 μM . The solution was heated to 80 $\text{^{\circ}}\text{C}$ for 10 min and then slowly cooled to 10 $\text{^{\circ}}\text{C}$ at a rate of 0.01 $\text{^{\circ}}\text{C}\text{,s}^{-1}$ using a thermal cycler (T-Gradient; Biometra), allowing the DNA nanostructures to self-assemble in a controlled manner. To prepare artificial cells with DNA nanostructures localized beneath the membrane, 2 μL of the aqueous solution containing DNA nanostructures was added to 40 μL of the TAP-in-hexadecane solution after sonication. Owing to electrostatic interactions between the negatively charged DNA nanostructures (hereafter referred to as DNA motifs) and the positively charged TAP monolayer, the DNA motifs were selectively localized beneath the lipid monolayer at the droplet interface.

5.4 | Micropipette aspiration

The mechanical properties of artificial cells were quantified using the classical micropipette aspiration technique. In this method, a glass micropipette with an inner radius much smaller than that of the target droplet is brought into contact with the droplet surface, and the lipid monolayer is aspirated into the pipette by applying a pressure difference P between the inside and outside of the pipette. The applied aspiration pressure induces a deformation of the interface, resulting in an aspiration length L inside the pipette. The mechanical properties of the interface were estimated from the relationship between the aspiration pressure P and the aspiration length L .

In this study, only droplets with radii $R \geq 20\text{ }\mu\text{m}$ were analyzed, and glass micropipettes with an inner radius of $R_p \approx 15\text{ }\mu\text{m}$ were used, corresponding to a geometric ratio of $R/R_p > 1.2$. Aspiration pressure and displacement were measured following a previously reported protocol [41]. Experiments were performed on an inverted optical microscope (Axiovert 40CFL; Carl Zeiss) equipped with a micromanipulator system (MMO-202ND and MN-4; Narishige), a microinjector (IM-11-2; Narishige), and a differential pressure transducer (DP15; Validyne). The droplet radius R and aspiration length L were determined from optical microscopy images.

5.5 | Statistical Analysis

P – x curves obtained from micropipette aspiration experiments were analyzed using nonlinear least-squares fitting based on the analytical model described in Equation 14. For each individual droplet, the aspiration region was identified automatically from the displacement time series, and fitting was restricted to the regime $x = L/R_p \leq 1$, prior to the onset of relaxation or viscous flow. The fitting parameters, the area-stretching modulus K and the combined interfacial tension–bending parameter $\gamma_0 + \tilde{\kappa}$, were obtained by minimizing the residual sum of squares using the trust-region reflective algorithm implemented in Python (SciPy, curve-fit). To avoid convergence to local minima, the fitting procedure was repeated with 10 randomly generated initial parameter guesses within physically meaningful bounds, and the solution yielding the highest coefficient of determination (R^2) was selected. Fits with $R^2 < 0.98$ were excluded from further analysis.

For statistical comparison of fitted parameters across different lipid compositions or DNA nanostructure conditions, droplets were treated as independent samples. Prior to group-level analysis, outliers were removed separately for each condition using the interquartile range (IQR) criterion ($1.5 \times \text{IQR}$). Data are presented as box plots with individ-

ual data points overlaid, and sample sizes (n) are indicated in the figure legends. Pairwise comparisons between groups were performed using Welch's two-sided t -test, which does not assume equal variances. Statistical significance is indicated as $p < 0.05$ and $p < 0.01$, as specified in the figure captions. All data processing, fitting, and statistical analyses were conducted using custom Python scripts.

Data availability

The data that support the findings of this study are available from the corresponding author upon reasonable request.

Conflicts of interest

The authors declare no conflicts of interest.

Acknowledgements

This research was partially funded by the Japan Society for the Promotion of Science (JSPS) KAKENHI (grant numbers 22H01188, 24H02287 (M.Y.), the Japan Science and Technology Agency (JST) (grant numbers FOREST, JPMJFR213Y; CREST (JPMJCR22E1) (M. Y.)), and the World-Leading Innovative Graduate Study Program for Advanced Basic Science Course (WINGS-ABC) at the University of Tokyo (K. M.).

Supporting information

Supporting Information is available from the Wiley Online Library.

references

- [1] Discher DE, and Eisenberg A. Polymer vesicles. *Science*. 2002;297(5583):967–973.
- [2] Sackmann E. Supported membranes: scientific and practical applications. *Science*. 1996;271(5245):43–48.
- [3] Seifert U. Configurations of fluid membranes and vesicles. *Advances in Physics*. 1997;46(1):13–137.
- [4] Lingwood D, and Simons K. Lipid rafts as a membrane-organizing principle. *Science*. 2010;327(5961):46–50.
- [5] Dimova R, and Marques C. The giant vesicle book. CRC Press; 2019.
- [6] Gudyka J, Ceja-Vega J, Krmic M, Porteus R, and Lee S. The Role of Lipid Intrinsic Curvature in the Droplet Interface Bilayer. *Langmuir*. 2024;40(22):11428–11435.
- [7] Jin Y, Liu D, and Hu J. Effect of surfactant molecular structure on emulsion stability investigated by interfacial dilatational rheology. *Polymers*. 2021 4;13.
- [8] Kim DH, Costello MJ, Duncan PB, and Needham D. Mechanical properties and microstructure of polycrystalline phospholipid monolayer shells: Novel solid microparticles. *Langmuir*. 2003;19(20):8455–8466.
- [9] Tsang KY, Lai YC, Chiang YW, and Chen YF. Coupling of lipid membrane elasticity and in-plane dynamics. *Physical Review E*. 2017;96(1):012410.
- [10] Mangiarotti A, Sabri E, Schmidt KV, Hoffmann C, Milovanovic D, Lipowsky R, et al. Lipid packing and cholesterol content regulate membrane wetting and remodeling by biomolecular condensates. *Nature Communications*. 2025;16(1):1–20.

[11] Santinho A, Chorlay A, Foret L, and Thiam AR. Fat inclusions strongly alter membrane mechanics. *Biophysical journal*. 2021;120(4):607–617.

[12] Chrysanthou A, Bosch-Forte M, Nadal C, Zarbakhsh A, and Gautrot JE. Interfacial mechanics of β -casein and albumin mixed protein assemblies at liquid-liquid interfaces. *Journal of Colloid and Interface Science*. 2024;674:379–391.

[13] Bujold KE, Lacroix A, and Sleiman HF. DNA nanostructures at the interface with biology. *Chem*. 2018;4(3):495–521.

[14] Shen Q, Grome MW, Yang Y, and Lin C. Engineering lipid membranes with programmable DNA nanostructures. *Advanced biosystems*. 2020;4(1):1900215.

[15] Kaletta N, Burick S, Qudbuddin Y, and Schwille P. Designing Tunable DNA Condensates to Control Membrane Budding Transformation in Synthetic Cells. *Advanced Science*. 2025 8;12.

[16] Rand RP, and Burton A. Mechanical properties of the red cell membrane: I. Membrane stiffness and intracellular pressure. *Biophysical journal*. 1964;4(2):115–135.

[17] Hochmuth RM. Micropipette aspiration of living cells. *Journal of Biomechanics*. 2000;33.

[18] Lee LM, and Liu AP. The application of micropipette aspiration in molecular mechanics of single cells. *Journal of Nanotechnology in Engineering and Medicine*. 2014 11;5.

[19] Waugh R, and Evans EA. Thermoelasticity of red blood cell membrane. *Biophysical Journal*. 1979;26:115–131.

[20] Guevorkian K, Colbert MJ, Durth M, Dufour S, and Brochard-Wyart F. Aspiration of biological viscoelastic drops. *Physical Review Letters*. 2010 5;104.

[21] Theret P, Levesque MJ, Sato M, Nerem RM, and Wheeler LT. The Application of a Homogeneous Half-Space Model in the Analysis of Endothelial Cell Micropipette Measurements. *Journal of Biomechanical Engineering*. 1988;110:190–199.

[22] Evans E, and Rawicz W. Entropy-driven tension and bending elasticity in condensed-fluid membranes. *Physical review letters*. 1990;64(17):2094.

[23] Evans E, and Rawicz W. Elasticity of "Fuzzy" Biomembranes. *Physical review letters*. 1997;79(12):2379.

[24] Henriksen JR, and Ipsen JH. Measurement of membrane elasticity by micro-pipette aspiration. *The European physical journal E*. 2004;14(2):149–167.

[25] Miller R, Li J, Bree M, Loglio G, Neumann A, and Möhwald H. Interfacial relaxation of phospholipid layers at a liquid–liquid interface. *Thin Solid Films*. 1998;327:224–227.

[26] Helfrich W. Elastic properties of lipid bilayers: theory and possible experiments. *Zeitschrift für Naturforschung c*. 1973;28(11-12):693–703.

[27] Fournier JB, and Galatola P. Corrections to the Laplace law for vesicle aspiration in micropipettes and other confined geometries. *Soft Matter*. 2008;4(12):2463–2470.

[28] Rangamani P, Mandadap KK, and Oster G. Protein-induced membrane curvature alters local membrane tension. *Biophysical journal*. 2014;107(3):751–762.

[29] Dymond MK. Lipid monolayer spontaneous curvatures: A collection of published values. *Chemistry and Physics of Lipids*. 2021 9;239.

[30] den Otter WK, and Shkulipa S. Intermonolayer friction and surface shear viscosity of lipid bilayer membranes. *Biophysical journal*. 2007;93(2):423–433.

[31] Manna E, Barai M, Mandal MK, Sultana H, Bykov AG, Akentiev AV, et al. Composition, functionality and structural correlates of mixed lipid monolayers at air-water interface. *JCIS Open*. 2021;3:100022.

[32] Luna C, Stroka KM, Bermudez H, and Aranda-Espinoza H. Thermodynamics of monolayers formed by mixtures of phosphatidylcholine/phosphatidylserine. *Colloids and Surfaces B: Biointerfaces*. 2011;85(2):293–300.

[33] Seto H, Nagao M, and Kawabata Y. Pressure-dependence of the bending modulus of surfactant monolayers in ternary microemulsion systems observed by neutron spin echo. *Colloids and Surfaces A: Physicochemical and Engineering Aspects*. 2006;284:430–433.

[34] Rekvig L, Hafskjold B, and Smit B. Chain length dependencies of the bending modulus of surfactant monolayers. *Physical review letters*. 2004;92(11):116101.

[35] Yanagisawa M, Yoshida Ta, Furuta M, Nakata S, and Tokita M. Adhesive force between paired microdroplets coated with lipid monolayers. *Soft Matter*. 2013;9(25):5891–5897. Available from: <https://doi.org/10.1039/C3SM50938A>.

[36] Kurokawa C, Fujiwara K, Morita M, Kawamata I, Kawagishi Y, Sakai A, et al. DNA cytoskeleton for stabilizing artificial cells. *Proceedings of the National Academy of Sciences*. 2017;114(28):7228–7233.

[37] Daly ML, Nishi K, Klawo SJ, Hinton KY, Gao Y, and Freeman R. Designer peptide–DNA cytoskeletons regulate the function of synthetic cells. *Nature Chemistry*. 2024;16(8):1229–1239.

[38] Ganar KA, Honaker LW, and Deshpande S. Shaping synthetic cells through cytoskeleton-condensate-membrane interactions. *Current Opinion in Colloid & Interface Science*. 2021;54:101459.

[39] Landau LD, and Lifshitz EM. *Theory of Elasticity*. vol. 7 of Course of Theoretical Physics. 3rd ed. Elsevier; 2012.

[40] Himbert S, D'Alessandro A, Qadri SM, Majcher MJ, Hoare T, Sheffield WP, et al. The bending rigidity of the red blood cell cytoplasmic membrane. *PLOS ONE*. 2022;17(8):e0269619. Available from: <https://doi.org/10.1371/journal.pone.0269619>.

[41] Sakai A, Murayama Y, and Yanagisawa M. Cyclic Micropipette Aspiration Reveals Viscoelastic Change of a Gelatin Microgel Prepared Inside a Lipid Droplet. *Langmuir*. 2020;5;36:5186–5191.

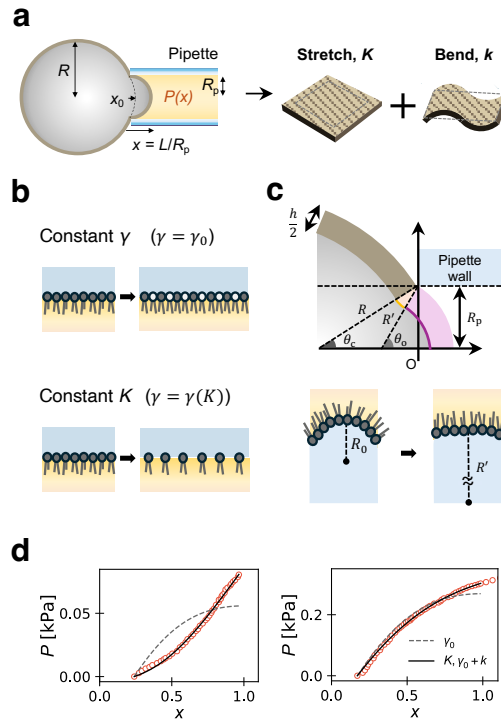


FIGURE 1 Analytical model for the deformation of membrane-covered spherical droplets during micropipette aspiration. (a) A droplet with radius R is aspirated by a pipette with an inner radius R_p under a certain pressure difference P between the external environment and the interior of the pipette. The resulting deformation in the aspirated region includes the surface stretching and bending due to the aspiration length L . Stretching and bending are characterized by an area-stretching modulus K and a bending modulus k , respectively. (b) Two different molecular-level scenarios of the interface during surface stretching: (Top) When the lipid supply rate from the reservoir is sufficiently fast compared to deformation time, the interfacial tension γ is maintained to be constant ($\gamma = \gamma_0$), and (Bottom) when the supply rate is slow, the strain is constant (constant area-stretching modulus, K), but γ varies with expansion ($\gamma = \gamma(K)$). (c) Curvature change of the lipid membrane: (Top) The schismatic of the neutral surface of the lipid membrane with a thickness h in the aspirated region inside the pipette. Curvature variations mainly arise in the aspirated spherical segment (purple) and the pipette edge (yellow). (Bottom) Considering the spontaneous curvature of lipids (curvature radius R_0), curvature changes from the initial $1/R_0$ to $1/R'$ in the aspirated spherical segment. (d) Two typical experimentally obtained P - x curves (red; left: convex-downward, right: convex-upward) and their fits using our model based on Equation 14 (black solid lines) and the conventional fits with a constant γ_0 (black dashed lines).

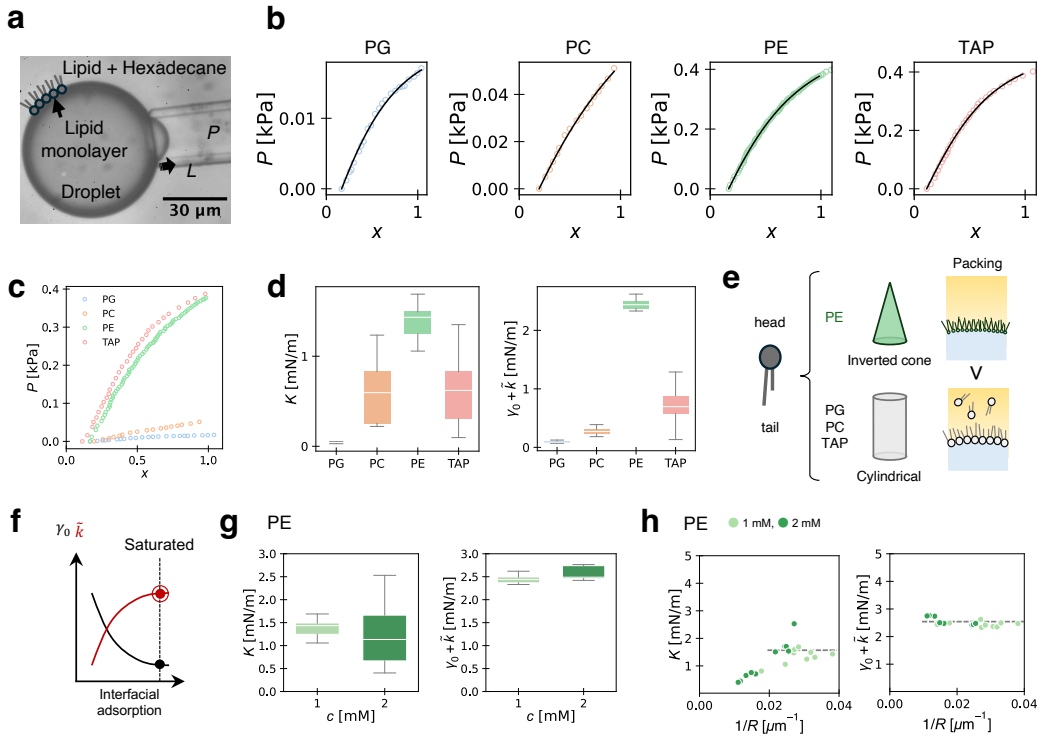


FIGURE 2 Micropipette aspiration of droplets with different types of lipids. (a) A microscope image showing a droplet aspirated by a pipette with $R_p = 12 \mu\text{m}$ at an aspiration pressure, P . (b, c) Typical P - x curves for droplets with each lipid (circles) and their fits using our model based on Equation 14 (black solid lines). (d) K (left) and $\gamma_0 + \tilde{k}$ (right) for each lipid droplets. PE shows the largest values both in K and $\gamma_0 + \tilde{k}$. ($n = 6, 7, 9$ and 25 for PG, PC, PE and TAP, respectively). (e) Schematics illustrating lipid molecular geometry and their adsorption at the interface. PE has a relatively small headgroup cross-sectional area compared with its hydrophobic tails, i.e. inverted-cone geometry. PC, PG, and TAP possess comparable head and tail cross-sectional areas, i.e. cylindrical lipids. Upon adsorption onto a surface with a large radius of curvature, PE molecules are easily packed on the membrane with small headgroups, resulting in an increased surface number density compared with the other lipids. (f) Schematic illustration of the opposite dependence of γ_0 and \tilde{k} on interfacial adsorption. While increasing interfacial adsorption generally reduces γ_0 , it simultaneously enhances \tilde{k} . When the spontaneous curvature c_0 of the adsorbed molecules is larger, \tilde{k} is shifted to higher values. (g) K (left) and $\gamma_0 + \tilde{k}$ (right) for PE droplets at two different lipid concentrations. The absence of any significant change in either parameter indicates that the interfacial adsorption of PE is already saturated at 1 mM. (h) The curvature dependency of K (left) and $\gamma_0 + \tilde{k}$ (right) for PE droplets. Light gray dashed lines indicate the average values. The dashed line for K is calculated using data with $1/R \geq 0.02 \mu\text{m}^{-1}$.

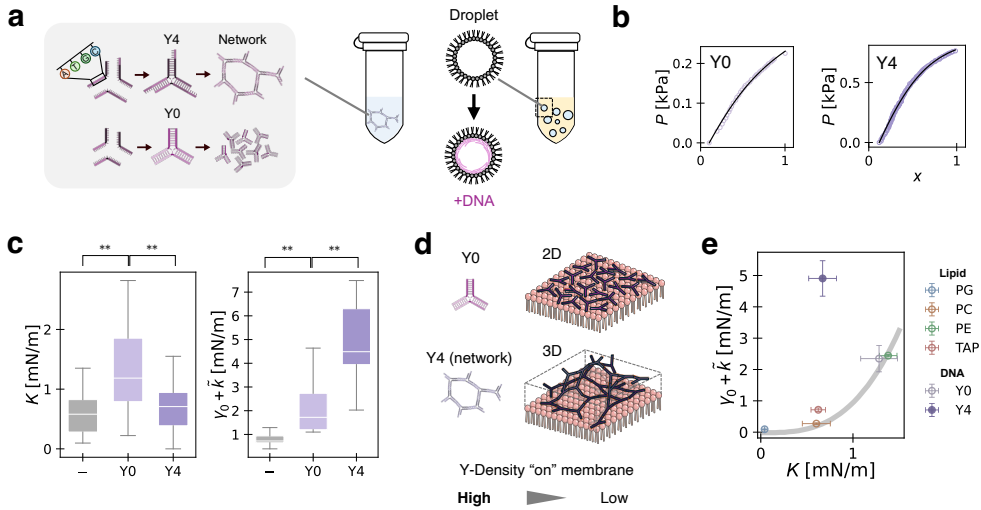


FIGURE 3 (a) Schematics of hybridization of DNA with and without sticky ends by decreasing the temperature. The three different DNA oligomers form a Y-shaped dsDNA motif. In the presence of sticky ends, the Y-motif DNAs further hybridize to create a network structure, whereas motifs without sticky ends remain isolated. These nanostructures electrostatically localize beneath the membrane when encapsulated within lipid-coated droplets. (b) Typical P - x curves for droplets with DNA nanostructures (circles) and their fits using our model based on Equation 14 (black solid lines). (c) K (left) and $\gamma_0 + \bar{k}$ (right) for each DNA nanostructures (Y0 and Y4). For reference, the DNA-free values (-) obtained for 1 mM TAP in the previous section are also shown ($n = 25, 16$ and 10 for -, Y0, and Y4, respectively). (d) Schematics of Y0 and Y4, which are confined in quasi-two-dimensional and three-dimensional configurations, respectively. Despite having the same total number of DNA motifs, the effective surface density of DNA motifs directly adsorbed at the interface is higher for Y0 than for Y4. (e) The average values of K and $\gamma_0 + \bar{k}$ for Y0 and Y4 with those of different lipids (obtained from Figure 2d). The error bars represent the standard error. A light gray line indicates the scaling relation, $\propto K^3$, expected from thin-film elasticity theory.